



Title	In-situ Observation Techniques of Solidification and Phase Transformation during Welding
Author(s)	Komizo, Yu-ichi
Citation	Transactions of JWRI. 2011, 40(2), p. 7-20
Version Type	VoR
URL	<a href="https://doi.org/10.18910/6265">https://doi.org/10.18910/6265</a>
rights	
Note	

*The University of Osaka Institutional Knowledge Archive : OUKA*

<https://ir.library.osaka-u.ac.jp/>

The University of Osaka

# In-situ Observation Techniques of Solidification and Phase Transformation during Welding<sup>†</sup>

KOMIZO Yu-ichi\*

## Abstract

*In order to respond to request for the direct observation of microstructure formation during welding, “in-situ observation techniques” are outlined in the present paper. They include the high-temperature laser scanning confocal microscopy (LSCM), the in-situ SEM which consists of the microstraining system compatible with EBSD measurements, the in-situ SIM, the spatially resolved X-ray diffraction (SRXRD), the time-resolved X-ray diffraction (TRXRD) and the hybrid system with LSCM and TRXRD. They can be applied to the analysis of microstructural changes for improving control of weld properties. When combined with additional experiments and modelling, these techniques enable a deeper understanding of the kinetics of phase transformations.*

**KEY WORDS:** (In-situ observation) (solidification) (phase transformation)  
(laser scanning confocal microscopy) (X-ray diffraction)

## 1. Introduction

The microstructures of welds are formed through various thermal cycles depending on the details of the welding path, including heat input, composition and so on. Thus, it is not easy to estimate the process of microstructure formation during the thermal cycle of welding. The crystal structure of low carbon steel transforms twice ( $\delta \rightarrow \gamma \rightarrow \alpha$ ) from liquid phase to room temperature. This provides an opportunity to obtain various desirable properties of a weld (the weld metal and the heat-affected zone (HAZ)) through microstructural control. Therefore, understanding the behaviour of phase transformation in the welding process is essential. These phenomena occur during rapid heating and cooling cycles (several hundred degrees/second) at high temperature—it is not easy to observe the phase transformation during welding in detail.

In order to analyze the microstructure change during welding, a lot of experimental methods have been applied. The major method is quenching. In the case of the quenching method by using liquid tin[1], the weld bead is frozen in a liquid tin bath during the welding process. Then the microstructure change in diffusion phase transformation is stopped. Analyzing solidification microstructure is possible for some sorts of alloy, by using this method. However, the experiment is time-consuming in order to analyze the microstructure at several temperatures.

In order to respond to the request for the direct

observation of microstructure formation during welding, “in-situ observation techniques” are outlined in the present paper.

## 2. High temperature LSCM system

High-temperature laser scanning confocal microscopy (HLSCM) is a candidate for such a tracking technique. The system consists of a laser scanning confocal microscope (LSCM) and infrared furnace. A schematic illustration of the system is shown in **Fig. 1**[2]. In confocal microscopy, laser light is focused by an objective lens onto the specimen. Using a confocal pinhole, only light incident from the focal plane is permitted to pass through to the photon detector. Hence, an extremely thin optical section is created, providing a high-resolution image. Because thermal radiation is also blocked by the confocal pinhole, only the polarized reflection of the high-intensity laser beam reaches the image sensor, resulting in a sharp image. The specimens, 5 mm in diameter and 1 mm in thickness, were placed in an alumina crucible and held in a platinum holder, which was inserted into the furnace. The temperature, measured by a thermocouple incorporated into the crucible holder, was displayed on a monitor and simultaneously recorded with the image at a rate of 30 frames/sec. The infrared-light focus in the furnace covers a volume at constant temperature 10 mm in diameter and 10 mm in height. The position of the specimen in the furnace is set into this volume. Simulated thermal cycles of welds are

<sup>†</sup> Received on December 26, 2011

\* Professor

Transactions of JWRI is published by Joining and Welding Research Institute, Osaka University, Ibaraki, Osaka 567-0047, Japan

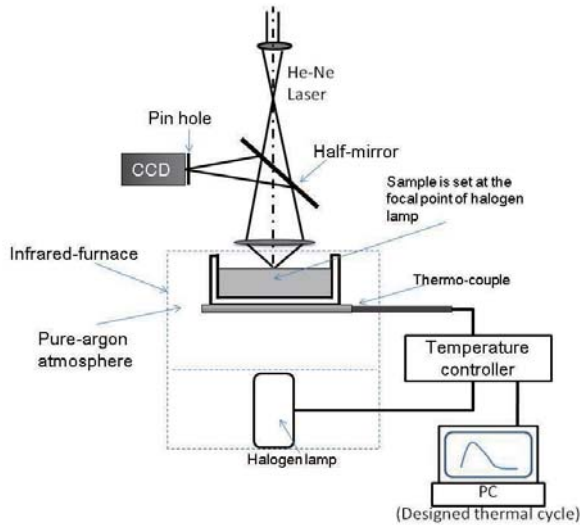


**Fig. 1** Schematic illustration of infrared furnace and laser scanning confocal microscopy. [2]

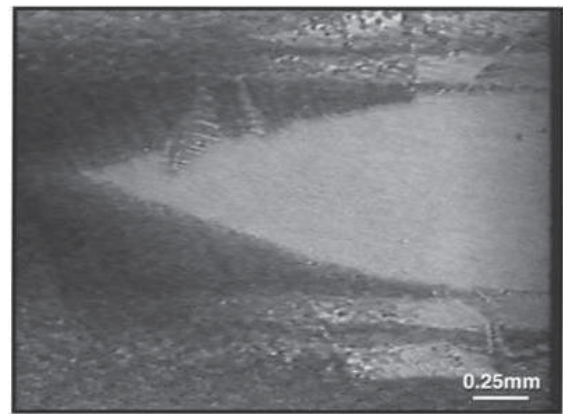
designed and input to the controller via a personal computer. A temperature controller (proportional-integral-derivative controller) reproduces such a designed thermal cycle by adjusting the on-off signal of a halogen lamp by monitoring the substrate temperature. The infrared furnace is suitable for simulating the thermal cycles of welds due to its highly temperature-responsive nature. Examples of LSCM images for various steel and thermal cycles are shown in the following section.

## 2.1. Solidification behaviour

The system is used for observation of the solidification behavior of steel[3-5], observation of sulfide formation in steel[6-8], determination of inclusion solubility[9], derivation of the interface migration rate during phase transformations of steel[10], observation of morphology of the interface during phase transformations of steel[11], tracking the dissolution behaviour of inclusions in slag liquid[12] and so on.

Trivedi et al selected a succino-nitrile-1.2 wt% acetone as an alloy analogy and were able to observe the solidification process in real time as shown in **Fig. 2**[13]. This observation enabled clear characterization of particle selection phenomenon, epitaxial growth, grain boundaries, and formation of porosity during welding. **Figure 3** shows the dark bands between the cellular crystals which were traces of perturbation motion of the crystal boundaries that moved up and down within the boundaries[3]. **Figure 4** shows the peritectic reaction and transformation of Fe-0.42%C alloy during isothermal holding at 1765K[14]. The  $\gamma$  phase grew along the periphery of the  $\delta$  crystals, completely covering the periphery after 0.2 seconds ( Fig.4(b) ), further grew into the  $\delta$  crystals and toward liquid.

**Figure 5** shows snapshots of LSCM observations for the solidification of high-strength steel (0.05 C–0.16 Si–1.65 Mn–0.011 Nb mass%) at a constant temperature of 1544 °C[15]. A temperature gradient was formed



**(a)**



**(b)**

**Fig. 2** Photographs showing branched dendrites growing from the interface and the roughness of the interface in succinonitrile + acetone system. [13]

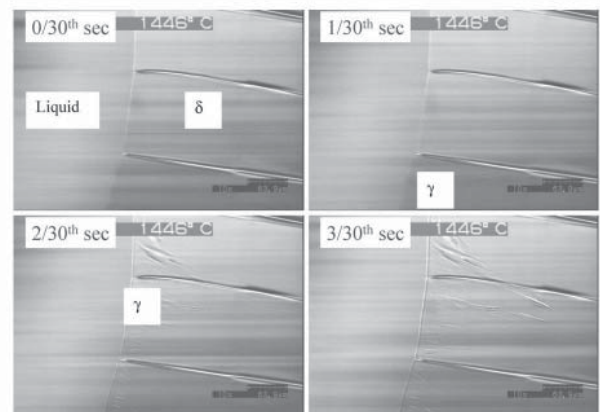


**Fig. 3** Melt/plamar crystal interface of 0.17%carbon steel. [3]

under the concentric solidification condition. The solidification phase was delta-ferrite and the interface morphology between liquid and solid had a cell-like pattern. Regrettably, the temperature gradient was too high for dendrite solidification, which is frequently

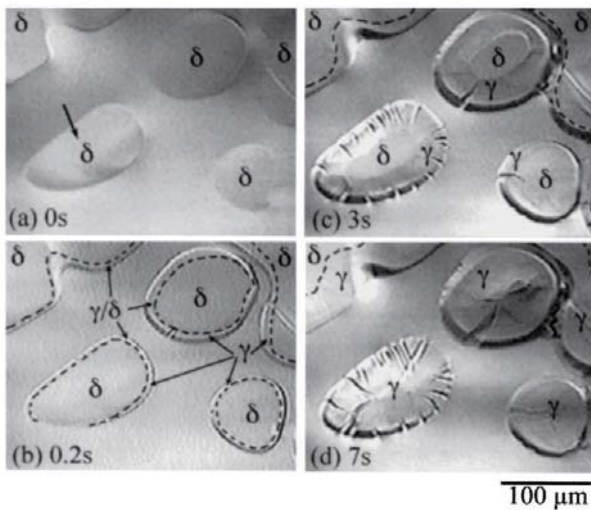


**Fig. 4** Peritectic reaction and transformation of Fe-0.42 %C alloy during isothermal holding at 1765K. [14]

observed as a solidification front during gas-tungsten arc welding of alloy steel.

## 2.2 $\delta \rightarrow \gamma$ transformation in carbon steel

The morphological instability of the interphase boundary during phase transformation in steels is an important issue for steelmakers to thoroughly understand the evolution of microstructures in processing. The appearance of the  $\gamma$ -phase in the  $\delta$  matrix at the beginning of the  $\delta \rightarrow \gamma$  transformation was observed as shown in Fig. 6[11]. The surface cells of the  $\gamma$ -phase formed at the triple point of  $\delta$  grain boundaries and at the  $\delta$  grain boundary.

Figure 7 shows snapshots of LSCM observations for the solid-state transformation process (delta-gamma) of high-strength steel (0.05 C–0.16 Si–1.65 Mn–0.011 Nb mass%) during the cooling cycle[15]. The delta-ferrite grain boundary was clearly observed due to thermal etching at high temperature, as shown in Fig. 7 (a). As the temperature decreases, a morphology with a wavy pattern developed, as shown in Fig. 7 (b) with weak contrast, and austenite grains formed. Immediately after the phase transformation, inclusions were formed at the grain boundary of the austenite, as shown in Fig. 7 (d). Analysis of their chemical composition revealed that they were manganese sulfides.

## 2.3 Grain growth and pinning effect

Figure 8 shows an example of grain migration observed in low carbon steel heated up to 1370 °C[26]. Figure 9[27] shows the in-situ observation images for pinned and migrating grain boundary of  $\beta$  - titanium. The applied thermal cycle was isothermally held at 1250 °C. The arrows show pinned grain boundary by inclusions and the dashed line was imposed on the migrating grain boundary. Even if long isothermal holding (92 sec) was applied to the sample at 1250 °C, the pinned grain boundary was not migrating. After the isothermal holding,

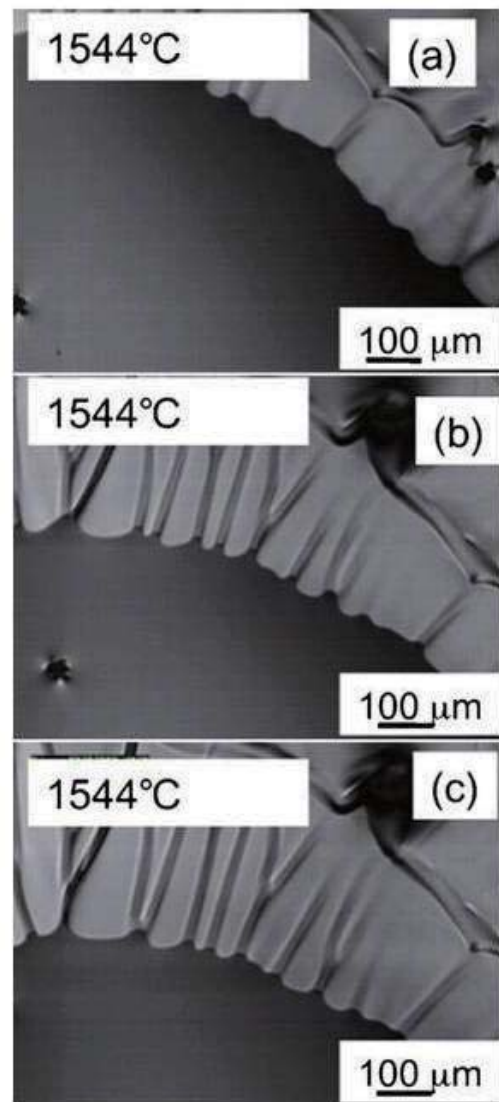


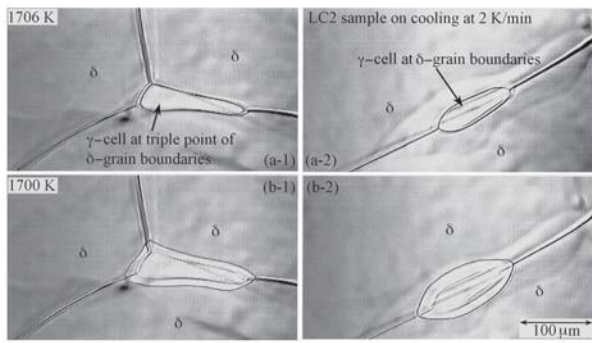
**Fig. 5** Snapshots of LSCM observations for a solidifications of high strength steel at a constant temperature of 1544. [15]

$\beta$  -grain size changed to 0.1 mm. On the other hand,  $\beta$ -grain size for the sample without inclusions in the same experimental conditions resulted in much larger  $\beta$  -grain size (about 6 mm).

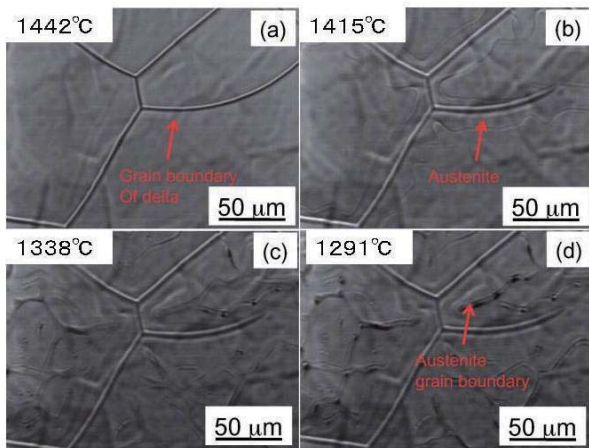
## 2.4 $\gamma \rightarrow \alpha$ transformation in steel

Figure 10 shows snapshots of LSCM observations for Fe-0.12 C steel during the cooling cycle (–1.7 °C/sec). At about 720 °C, allotriomorphic ferrite developed along austenite grain boundaries. The contrast of the allotriomorphic ferrite was very weak compared to that of microstructure with surface-relief. After that, at about 690 °C, the morphology of the interface changed, and well-aligned ferrite plates (Widmanstätten ferrite) developed, with austenite retained between the plates. The balance of anisotropic interface energy and





**Fig. 6** The surface cells of the  $\gamma$ -phase formed at the triple point of  $\delta$ -grain boundary. [11]



**Fig. 7** Snapshots of LSCM observations for solid state transformation ( $\delta$ - $\gamma$ ) in 0.05% C -0.16% Si -1.65% Mn -0.011% Nb steel. [15]

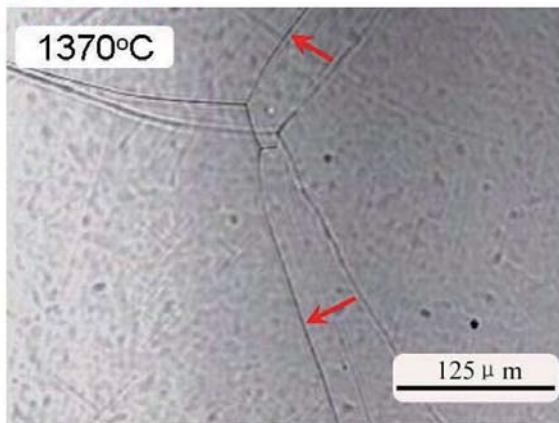


**Fig. 8** Grain boundary migration in austenite phase. [26]

segregation behaviour of solute elements determines the growth behaviour of the ferrite plates[15].

**Figure 11**[25] shows the in-situ observation of the nucleation of bainitic ferrite in Fe-0.15 C steel during the cooling cycle ( $-8^\circ\text{C}/\text{sec}$ ). The transformation begins at the cooling boundary, as shown in Fig. 11. Austenite grain boundaries are effective nucleation sites for bainitic ferrites.

**Figure 12**[28] shows the in-situ morphological evolution of bainite transformation. It is noteworthy that the nucleation sites of bainite can be classified into the following two categories: grain boundaries and inclusions, where primary bainitic ferrite nucleates, and the surface of primary bainitic ferrite, where sympathetic nucleation occurs. The bainitic ferrites increased rapidly by sympathetic nucleation, finally resulting in impingement between them. Their interlocking nature and impingement are directly shown in Fig. 12. As shown in the figure, the bainitic ferrites causing impingement were parallel to each other and grew in the same direction as the primary bainitic ferrite.

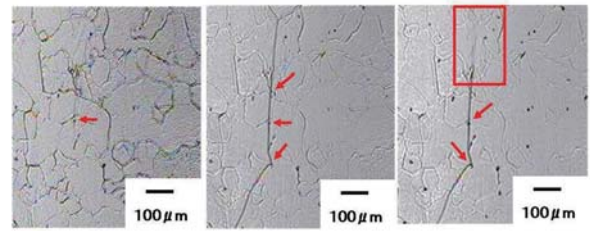


**Fig. 9** Pinning of grain boundary migration by small particles. [27]

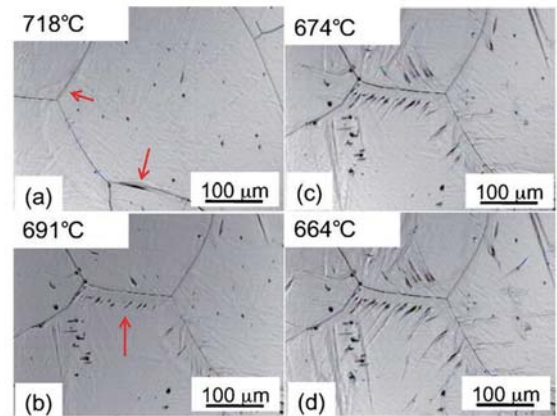


**Fig. 10** Allotriomorphic ferrite developed along austenite grain boundaries. [15]



**Fig. 11** Nucleation of bainitic ferrite in Fe-0.15% C steel.

[25]

## 2.5 Effect of inclusions on the nucleation of intragranular acicular ferrite

As an example of in-situ observation with HLSCM, nucleation and growth behavior of acicular ferrite in the weld metal (low carbon -Ti-B system) are shown in Figs. 13 and 14. In Fig.13[16], the arrow shows a morphological change corresponding to acicular ferrite nucleation and growth. The arrow direction corresponds to the observed growing direction. It was clear that the grain boundaries of austenite did not serve as a nucleation site because the segregation of boron at the grain boundaries can reduce the grain boundary energy to transform from the grain boundary. The morphological change corresponding to intragranular nucleation and growth of acicular ferrite started as indicated by the arrows. The direct evidence for nucleating and growing at inclusion site is shown in Fig.14<sup>[16]</sup>. It was clearly shown that the acicular ferrite grew from the inclusions.

Figure 15[29] shows the schematic illustration for metallurgical phenomena around an inclusion. The inclusions which related to acicular ferrite formation were multi-phase and surrounded by TiO. The Baker-Nutting orientation relationship was satisfied between the TiO and acicular ferrite. The Kurdjumov-Sachs orientation relationship was satisfied between the acicular ferrite and austenite.

## 2.6 Martensite transformation

Figure 16[31] shows the in situ observations of the martensite transformation behaviour of an austenite grain during the cooling cycle in 13Cr-9Ni-0.5Mo steel. As shown in Fig. 16(a), original grain was observed as

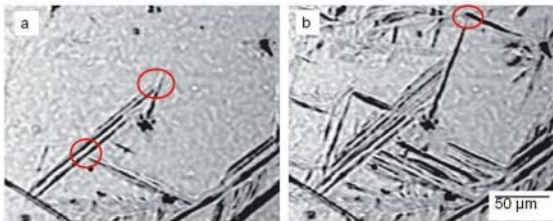


Fig. 12 Growth and impingement of bainitic ferrite. [28]

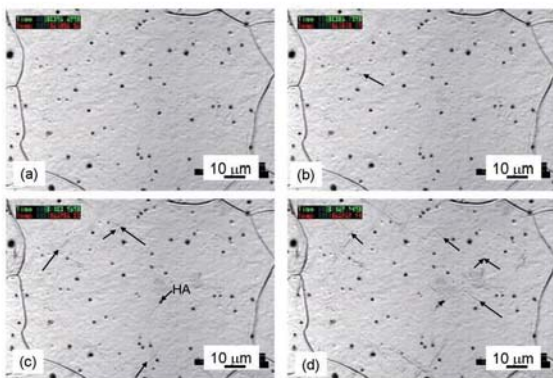


Fig. 13 Acicular ferrite nucleation and growing from

oxide inclusions in low carbon Ti-B weld metal. [16] austenite grains at 135°C. The surface relief of the martensite structure is shown in Fig. 16(b). At the lower part of the grain in Fig. 16(d), the remained austenite can be clearly observed among the blocks that had transformed earlier (shown as white dotted lines). With decreasing temperature, the formation of the blocks and packets was clearly observed and groups of laths were formed in packets, as shown by the arrows in Fig. 16(e). Finally, the remained austenite in each packet was gradually transformed into martensite laths, as shown in Fig. 16(h).

A model of lath martensite transformation is proposed from the results shown in Fig. 17[31]. Initially, in one packet, a block that has a preferred variant from the energy viewpoint is transformed from the austenite grain boundary. Then, the block of another packet appears from another austenite grain boundary. The two blocks collide as shown in Fig. 17(b). Another variant of another packet that belongs to the same bain correspondence is formed from the deformed austenite to immediately relax the transformation strain [Fig. 17(c)]. Moreover, because this

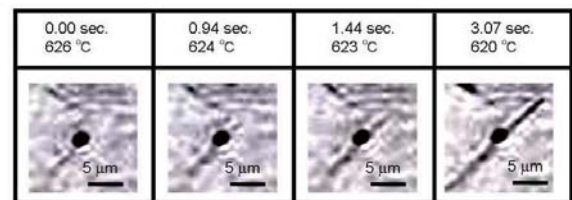


Fig. 14 Acicular ferrite nucleating and growing at inclusion site. [16]

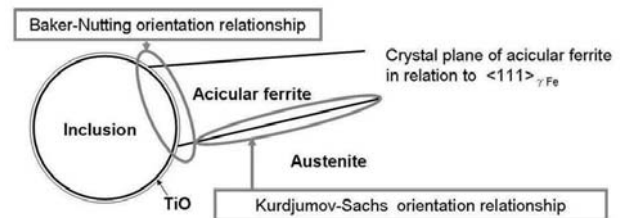


Fig. 15 Schematic illustration for metallurgical phenomena around inclusion for acicular ferrite formation. [29]

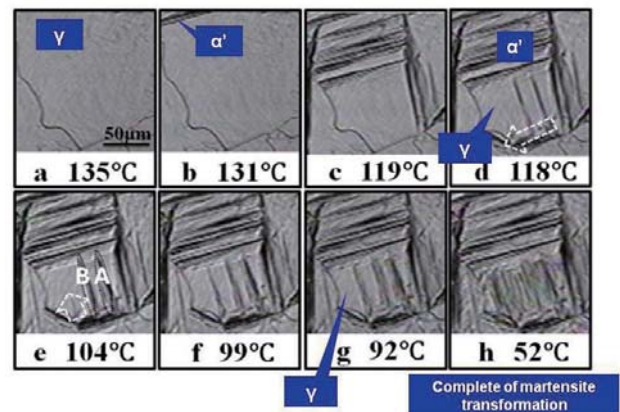


Fig. 16 In-situ observation results for martensite transformation in an austenite grain. [31]



block has a preferred variant from the energy viewpoint, it is suggested that the other block is formed apart from the first block to relax the transformation stress [Fig. 17(c)]. In the next stage, the self-accommodation variant (another block in the same packet) is dominant because the amount of austenite is decreased. Therefore, the martensite phase is formed around the initial block as a self-accommodation variant [Figs. 17 (d) and (e)]. Finally, transformation occurs among the neighbours of the transformed martensite block.

### 3. In-situ observation by SEM

Electron microscopists recognized early on that many challenges in materials science, some of them related to phase transformation and failure mechanisms, required experiments involving real time observation of the studied material subjected to specific conditions, such as atmospheric pressure, temperature, electrical or magnetic fields, and load, among others. This led to the rise of in situ electron microscopy experimentation[34-37]. **Figure 18** shows the microstraining system compatible with EBSD measurements[38]. Dedicated equipment, such as the modified SEM chamber door with a tensile stage attached to it, has been developed to allow in situ EBSD data collection during straining experiments. **Figure 19**<sup>(38)</sup> shows two different grain boundaries on alloys ERNiCrFe-7 and ERNiCr-3 before and after the in situ SEM high temperature deformation test. Alloys ERNiCrFe-7 and ERNiCr-3 have a differentiated grain boundary (GB) morphology, presenting predominantly flat and undulated GBs, respectively.

### 4. In-situ observation by scanning ion microscopy

The microstructure was observed by scanning ion microscopy (SIM) imaging. The ferrite and austenite grains can be observed easily because the contrast of the SIM image is quite sensitive to the differences in crystal orientation, crystal structure and chemical compositions. **Figure 20**[39] shows the in situ SIM observation of the phase transformation around an inclusion existing at the inside of the specimen at 873K.

### 5. In-situ observation by Synchrotron radiation

Over the past decade, two synchrotron based techniques have been developed at Lawrence Livermore National Laboratory for direct observation of phase transformations induced by welding[40-51]. These techniques are spatially resolved X-ray diffraction (SRXRD), which was developed to map the phases that exist in the HAZ, and time-resolved X-ray diffraction (TRXRD).

#### 5.1 SRXRD

The SRXRD technique was developed to map the phases that exist in the HAZs of steady state moving arc welds. In this method, X-ray diffraction patterns are acquired in real time at discrete locations in the weld HAZ. These experimental data can then be analyzed and

modeled to understand the kinetics of phase transformations taking place under the steep temperature gradients and high peak temperatures associated with welding.

The experimental setup is summarized schematically in **Fig. 21**[52]. The synchrotron beam emerging from the

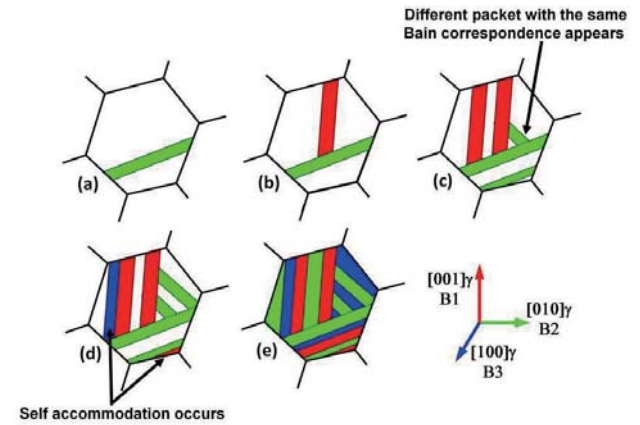


**Fig. 17** Schematic model describing the variant selection in martensite transformation. [31]

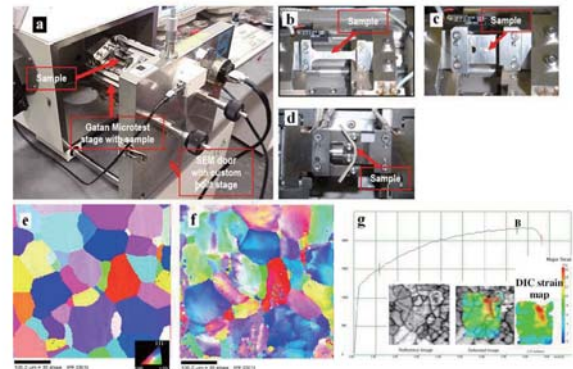


**Fig. 18** Microstraining system compatible with EBSD measurements. [38]

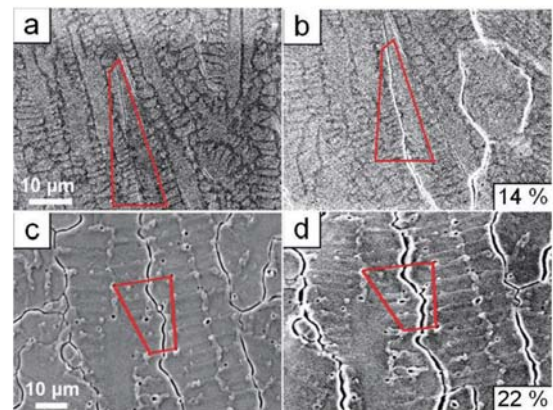


**Fig. 19** Grain boundaries on alloy ERNiCrFe-7(a,b) and ERNiCr-3(c,d) during in situ SEM high temperature

deformation tests. [38]

wiggler was focused by a toroidal mirror, passed through a 1 mm vertical entrance slit and monochromatized with a double Si(111) crystal. Results of a point-by-point phase mapping along the y-direction from the base titanium material into the HAZ are shown in Fig. 22[52]. In order spatially to resolve the phases in the HAZ of the titanium fusion weld under these conditions, a 0.25 mm (vertical) x 0.5 mm (horizontal) beam spot was used for the experiments.

The SRXRD process was successfully used to map the phases occurring in the HAZ of gas tungsten arc welds in AISI 1005 steel[47] and duplex stainless steel[50]. These measurements constitute the first *in situ* and direct experimental investigations of phase

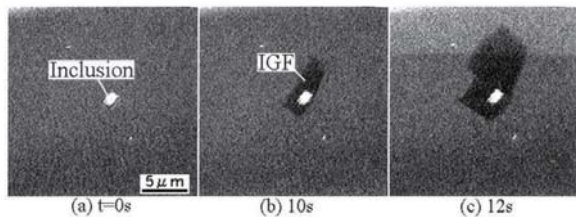


Fig. 20 In situ SIM observation of the phase transformation around an inclusion. [39]

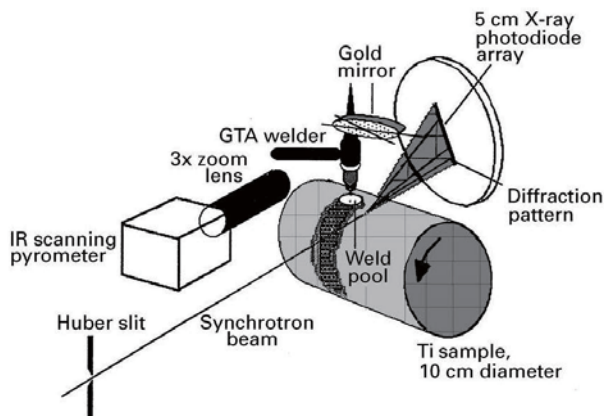


Fig. 21 Schematics of the SRXRD setup used for in situ phase mapping. [52]

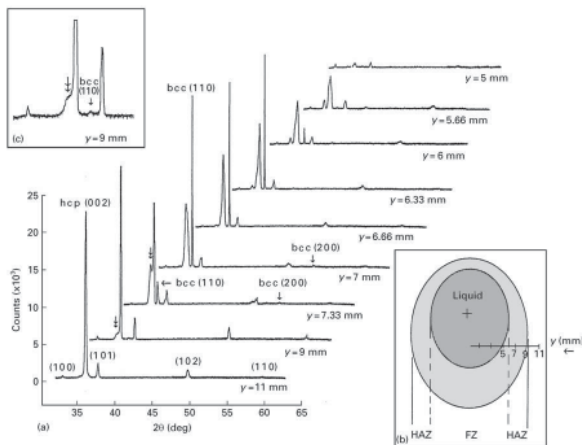


Fig. 22 Selected SRXRD diffraction patterns as a function of position in the HAZ of a titanium fusion

weld. [52]

transformations in steel welds, and the information contained within the HAZ phase map can be used to calculate phase transformation rates.

## 5.2 TRXRD

The related TRXRD technique was developed to analyze the transient arc welding conditions using rapid sampling X-ray diffraction to observe the phases that exist in the HAZ during rapid heating and cooling of the FZ and HAZ in real time. The transient welds heat and cool much more rapidly than steady state welds and require different data acquisition methods to achieve the high temporal resolution (50 to 100 ms) necessary to monitor the spot welds during heating and cooling.

Elmer et al.[46] showed that TRXRD could track phase transformation during welding in real time. Synchrotron radiation makes time-resolved diffraction measurements possible in local areas; phases that exist in the HAZ and fusion zone (FZ) of metal can be identified in real time. This technique was used to analyse the phase transformation during solidification of carbon-manganese (C-Mn) steel, and Babu et al.[49] verified the existence of non-equilibrium phases directly in the rapid cooling cycle of spot welds. In addition, TRXRD can be applied in tracking the phase evolution in the HAZ. The formation of the microstructures of duplex stainless steel (DSS)[50] and C-Mn[47] steel were observed in the thermal cycle of HAZ using TRXRD system. In experiments with DSS, the phase balance between ferrite and austenite was estimated, and the precipitation of the detrimental phase in the thermal cycle of the HAZ was assessed. In TRXRD experiments with C-Mn steel, the effect of transformation strain on the diffraction pattern profile during martensitic transformation was discussed.

### (1) Set-up for TRXRD at SPring-8

Our research group began TRXRD experiments for welding by developing a new technology for the system[18,26,33,53-62]. We focussed on the details of the weld solidification phenomena in the directional solidification process under rapid cooling because the influence of a preferred orientation was important for observing directional solidification along the  $\langle 100 \rangle$  direction towards the moving heat source.

The TRXRD experiments were performed in undulator beam line (BL46XU) in the third generation Synchrotron Radiation source, SPring-8 (JASRI). The schematic illustration of the TRXRD system is shown in Fig.23[60]. At undulator beam line, the X-ray was monochromatized with double Si crystals and the ultra-bright X-ray irradiated the fixed point on the welding bead. The welding torch position was the controlling parameter of the system. When torch arrived at decided positions, the shutter of X-ray in front of the X-ray slits was opened. After that, the exposure starting and exposure finishing signals could be set at the any point of torch positions. The slit size was 0.5x0.1 mm square. The time resolution was 0.01 seconds with a



two-dimensional X-ray camera. For the two-dimensional

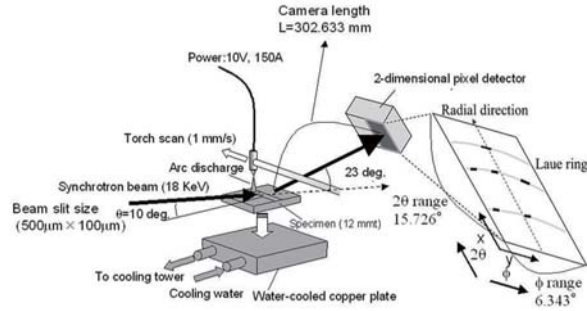


**Fig. 23** Schematic drawing of the time-resolved X-ray diffraction system using synchrotron radiation. [60]

camera, each pixel could count the photon count. The S/N ratio, dynamic range and read-out time for data is excellent with which a halo pattern of liquid phase during welding could be detected in the time-resolution of 0.01 seconds.

The sample was restrained on the water-cooled copper anode to avoid warping due to the plasma heating. These water-cooled copper anodes and the samples were set on the theta-axis of multi-axis goniometer, which was installed at 46XU beam line of SPring-8. The plasma torch driven system was integrated with the multi-axis goniometer and bead-on-plate welding was carried out on the prepared sample.

First, the solidification process was confirmed by SRXRD as a function of the distance from the weld pool, which was melted by an arc of the quenched metals after welding[13,14]. However, the observation of crystallization at a lateral resolution in relation to a time resolution of 0.1 s was impossible. That is, because the microstructure was ultimately static, understanding the crystallography during heating and cooling was not possible. For instance, the eutectic microstructure is formed in the liquid phase during solidification; the displacement of interplanar spacing by thermal expansion and shrinkage could not be observed. Next, the phase transformation was dynamically observed along a certain direction on the reciprocal space using an imaging plate[15-17]. A crystallinity change was observed with a temperature drop, and the growth of dendrites was captured. We assumed the rotation of dendrites from the discontinuous diffraction pattern recorded by the imaging plates along one direction of reciprocal space. However, eutectic growth in the remaining liquid phase was confirmed, though peritectic growth of the hetero phase on the primary phase was expected. Therefore, it was difficult to simultaneously observe the primary phase and the hetero phase along a certain direction because interfaces have coherency and preferred crystal orientation.

With the availability of intense X-ray beams from synchrotron storage rings, it is now possible to directly observe phase transformation and microstructural evolution *in situ* and in real time as a function of welding

time. Therefore, we developed a two-dimensional

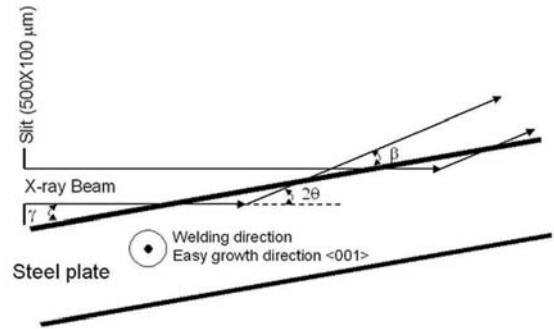


**Fig. 24** Scattering geometry and penetration depth estimation for X-ray. [60]

time-resolved X-ray Diffraction (2DTRXRD) system for real welding[18-28]. Weld metal rapid solidification was then dynamically observed at a time resolution of 0.01–0.1 s.

The scattering geometry for the experiments is shown in **Fig. 24**[60]. The slit size was W0.1 mm× L0.5 mm and the irradiated area resulting was 0.288 mm<sup>2</sup>. The penetration depth of X-rays can be calculated by using the relation:

$$\int_0^t \frac{I_0}{\sin \gamma} e^{-\mu x(1/\sin \gamma + 1/\sin \beta)} dx = G \cdot \int_0^\infty \frac{I_0}{\sin \gamma} e^{-\mu x(1/\sin \gamma + 1/\sin \beta)} dx$$

where  $I_0$  is intensity of incident beam,  $t$  is penetration depth,  $\mu$  is linear absorption coefficient,  $\gamma$  angle with the surface of steel plate made by incident beam,  $\beta$  angle with the surface of steel plate made by diffracted beam. With  $G = 0.99$ , the penetration depth of X-ray resulted in 16.91  $\mu\text{m}$ . Thus, the observation volume of the current experimental setup was  $5.29 \times 10^{-12} \text{ m}^3$ . **Figure 25** shows the penetration depth of X-ray in  $\delta$ -ferrite as a function of incident angle in the X-ray energy of 18 keV[60].

## (2) Solidification and phase transformation behaviour during welding

**Figure 26**[33] shows the solidification behaviour in 14Cr-6Ni steel. When the crystal reached to the irradiated area of X-ray during continuous growth, the phase was identified as shown in this figure. The broad pattern around delta-110 reflection is from weld pool (liquid metal). The halo pattern is direct evidence of in-situ observation of solidification process.

**Figure 27**[59] shows the AF mode austenitic stainless steel and Fe-0.88%C steel recorded with a two dimensional detector. AF mode means that the primary phase is fcc- $\gamma$  (austenite) and the secondary phase is bcc- $\delta$  (ferrite). In austenitic stainless steel, the  $\gamma$  phase crystallized first. Then, the diffraction spot blinks randomly with a temperature drop at about 1440 °C. After the diffraction of the  $\gamma$  phase was scattered like a ring, the diffraction of the  $\gamma$  phase condensed into the spot with an increase in the diffraction intensity of  $\delta$  phase. Finally, the surface orientation is formed with a

distribution of several degrees. This might mean that the

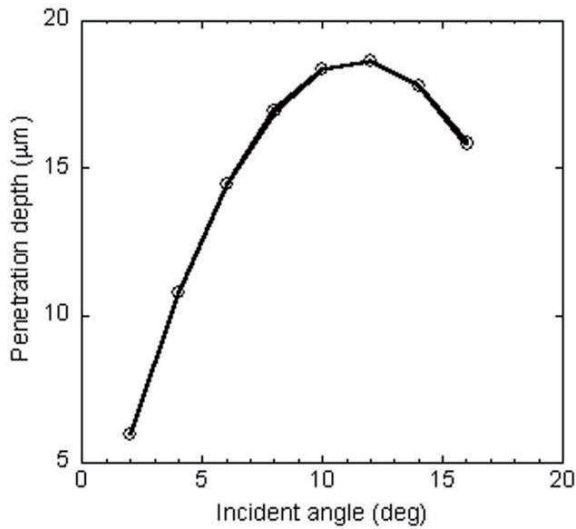


**Fig. 25** Penetration depth of X-ray in  $\delta$ -ferrite as a function of incident angle in the X-ray energy of 18 keV. [60]

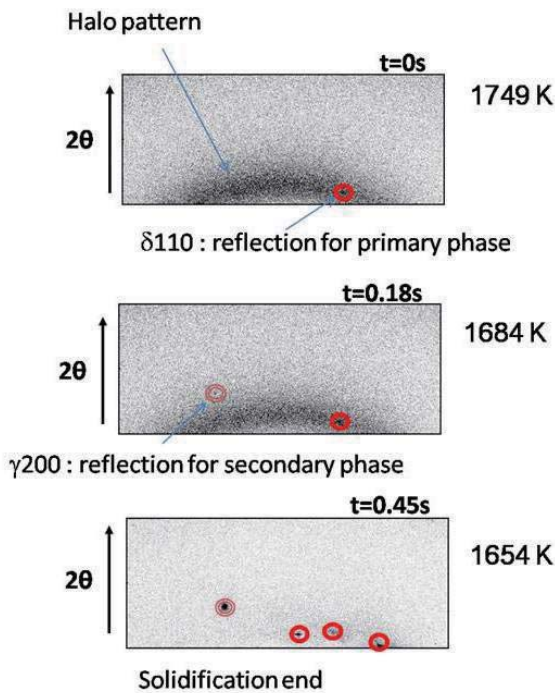


**Fig. 26** Primary and secondary phase from liquid in 14Cr-6Ni steel. [33]

lineage structure, by edge dislocation, formed in dendrites during rapid cooling. Further, the angle of  $\delta 200$  and  $\gamma 220$  is about  $5^\circ$ . This also corresponds to the K-S relationship. On the other hand, in 0.88%C steel, the diffraction pattern of the  $\gamma$  phase first appears at about  $1410^\circ\text{C}$ . At  $1130^\circ\text{C}$ , the diffraction spots of the  $\gamma$  phase extend in  $y$ -direction while the diffraction pattern of

secondary  $\alpha$  phase appears. These diffraction intensities of the  $\alpha$  phase gradually increase while the diffraction patterns of  $\gamma$  phase become weaker at  $750^\circ\text{C}$ . Finally, the diffraction pattern of the residual  $\gamma$  and  $\alpha$  phases mainly coexist at  $450^\circ\text{C}$ . The comparatively random microstructure is formed as shown by the continuous ring pattern. When the grain size is further reduced, the Laue spots merge into a general background and only Debye-Scherrer rings are visible.

**Figure 28**[59] shows the temperature dependency of the full width at half maximum (FWHM) in reciprocal space units and the lattice constant of the  $\gamma$  phase in the Fe-0.88%C. It should be noted that the dendrite grows mainly in a two step process. That is, the lattice constant decreases after a decrease of FWHM. There is no change at the solid phase transformation.

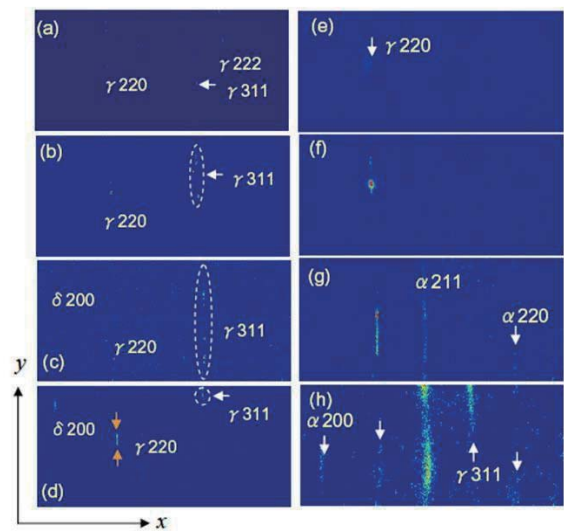


**Fig. 27** Typical TRXRD patterns of AF mode austenitic stainless steel (a-d) and hypereutectoid carbon steel (e-h). [59]

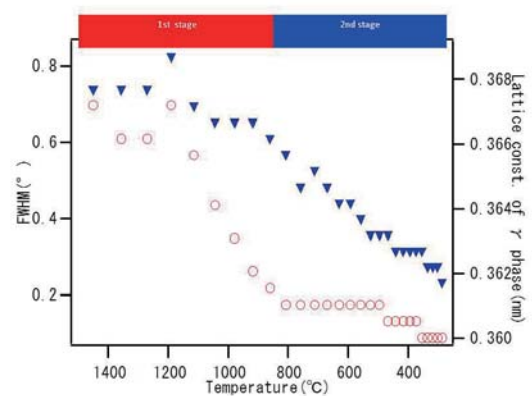


**Fig. 28** Temperature dependency of the full width of half maximum and the lattice constant of the austenite phase in Fe-0.88%C. [59]

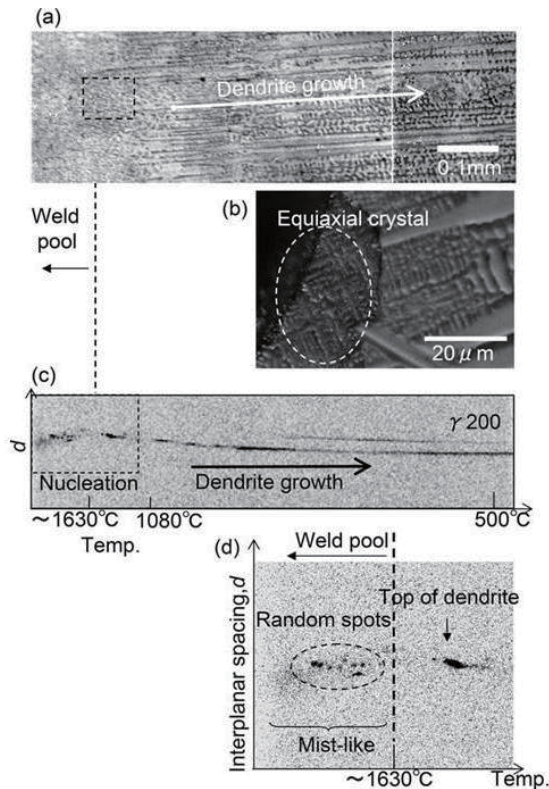


**Fig. 29** Microstructure of quenched AF mode stainless steel and diffraction pattern during the microstructure formation observed by the imaging plate. [69]

The crystal growth and the microstructure formation during rapid cooling have been examined. However, our main interest is the early solidification and the nucleation. The possibility of the observation of the nucleation is investigated. **Figure 29**[69] shows an example of the microstructure and the TRXRD pattern observed by moving IP in order to observe the microstructural formation along the radial direction of reciprocal lattice space. The boxes in (a) and (c) correspond to (b) and (d) zooming into details, respectively. Figure 29(a) is the microstructure of quenched AF mode stainless steel. Equiaxial crystals were observed between the weld pool and the top of dendrites as shown in Fig. 29(b). Figure 29(c) is a displacement of  $\gamma_{200}$  interplanar spacing in the stainless steel with the temperature drop observed on IP. The random spots and background like halo were observed in the weld pool as shown in Fig. 29(d). The background around random spots looks misty. Therefore, we describe it as the mistlike pattern. The mistlike pattern stands for the possibility of the embryo with a spatial and probability distribution. Furthermore, it is assumed that random spots correspond to equiaxial crystals by comparing with the microstructure shown in Fig. 29(b). The random spots, that have the different interplanar spacing, condensed into a spot with the dendrite growth, as shown in Fig. 29(d). Two intensity distributions in the broad diffraction pattern were observed in the early solidification[59]. Then, the crystallite sizes were

estimated as 1 and 5 nm by the Scherrer method, respectively. It was confirmed that it was roughly equal to a radius of the critical nucleus. It is assumed that this broad pattern corresponds to the mistlike pattern in this study. Finally, we explored possibilities that this mistlike pattern is the thermal diffuse scattering (TDS). The coherent scattering and the incoherent scattering appear as a halo pattern and the background, respectively, at a high temperature owing to the TDS. The influence of TDS on the diffraction peak of  $\gamma_{200}$  is small. Furthermore, the thermal strain was estimated about 1.5% at 1400 °C by the fraction of shrinkage. Thus, the possibility to observe the nucleation and the solidification by 2DTRXRD is expected by the further improvements.

In order to clarify the effect of tip velocity on the weld solidification process of hot-work tool steel (SKD61) during welding, information about microstructure evolution was obtained by the combination of a liquid tin quenching and time resolved X-ray diffraction technique using intense synchrotron radiation. Since the surface of the mould used for hot work or die-casting undergoes a hot-cold thermal cycle, heat check (thermal fatigue cracking) occurs due to thermal fatigue. To prevent this, composition planning is carried out so that no non-molten carbides remain during quenching. SKD61 has a high-content of molybdenum and vanadium in order to give it resistance to softening during tempering (heat resistance). **Figure 30**[61] is a calculation diagram prepared using Thermo-calc, a general-use thermodynamics calculation software. SKD61 passes the solidification process  $L \rightarrow L + \delta \rightarrow L + \delta + \gamma \rightarrow L + \gamma \rightarrow \gamma$  in a state of equilibrium. Thus, SKD61 is thought to experience FA mode solidification.

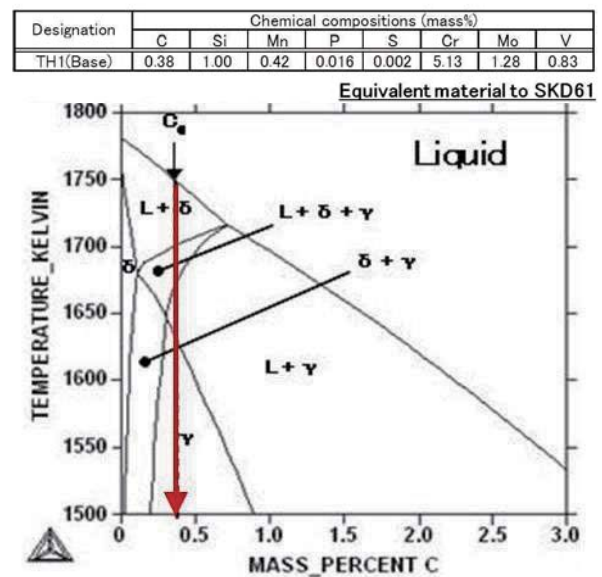


**Fig. 30** Binary phase diagram of tool steel calculated with Thermo-Calc. [61]



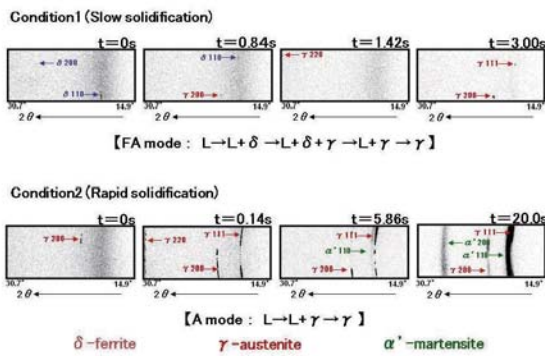


**Fig. 31** Chronological change of diffraction patterns in TRXRD with different solidification speed. [61]

The results of the in situ observations of the weld solidification process by the time-resolved X-ray diffraction system are shown in **Fig. 31**[61]. The horizontal axis corresponds to the diffraction angle and  $t$  is the elapsed time from the appearance of primary crystals. Under welding condition 1 (slow solidification), which simulate equilibrium solidification, the  $\delta$  phase appears as primary crystals. Subsequently, at  $t = 0.84$  s, the  $\gamma$  phase appears as the second phase and at  $t = 1.42$  s, the peritectic reaction is completed. The  $\delta - \gamma$  phase transformation generally depends on the presence of the Kurdjumov-Sachs (K-S) relationship and  $\delta 110 // \gamma 111$  and  $\delta 200 // \gamma 220$  commensurate interface formations were noted. Thus, SKD61 solidifies in the FA mode and is peritectic and this matches the solidification mode predictable from the calculated state diagram. These diffraction peak changes were detected along with a halo pattern, indicating the presence of a liquid phase, and it is thus possible to confirm the coexistence of both liquid and solid phases during solidification. Because of the appearance of a spotty pattern in the diffraction peaks, it is also thought that this surface orientation is due to unidirectional solidification. On the other hand, under welding condition 2 (rapid solidification), which simulate quench solidification, the  $\gamma$  phase appears as primary crystals and at  $t = 5.86$  s, a broad  $\alpha$  phase diffraction peak appeared. This broad peak means that the crystalline lattice is unevenly distorted. The detected  $\alpha$  phase is thought to be a bct phase (or  $\alpha'$  phase), which is approximately the same as  $2\theta$ . The surface orientation at the  $\gamma - \alpha'$  transformation corresponds to the K-S relationship, and the martensitic transformation starts at  $t = 5.86$  s. As this happens, the  $\gamma$  phase diffraction peak also is distorted and broadens. At  $t = 20$  s, the  $\gamma$  phase has not disappeared and finally a residual  $\gamma$  phase and a martensite phase coexist. It is thus clear that a mode transition occurs in SDK61 during quench solidification and that solidification is in mode A.

**Figure 32**[68] shows the single diffraction pattern of 14Cr5Ni steel for the martensite transformation of the cooling to room temperature. First  $\gamma 311$  diffraction

peak was detected as shown in Fig.32(a). During the martensite transformation the diffraction pattern was changed from the spot-like to ring-like. This can correspond to the rotation of austenite crystal.

## 6. Hybrid system with LSCM and TRXRD

With the availability of intense X-ray beams from synchrotron storage rings, it is now possible to directly observe phase transformation and microstructural evolution in situ and in real time as a function of welding time. Therefore, we developed a two-dimensional TRXRD system for real time observation of welding. **Figure 33**[33] shows a schematic illustration of the control flow for the in situ observations in real and reciprocal lattice space. The specimens, 5 mm in diameter and 1 mm in thickness, were placed in a BN crucible in which the X-ray absorption is quite small. The crucible was held by a platinum holder, which was inserted in the furnace. The temperature was measured by a thermocouple incorporated into the crucible holder. The specimens were placed at the focal point of a halogen lamp. The temperature controller, which was connected to a personal computer (PC), the thermocouple and the halogen lamp in the furnace were placed outside the

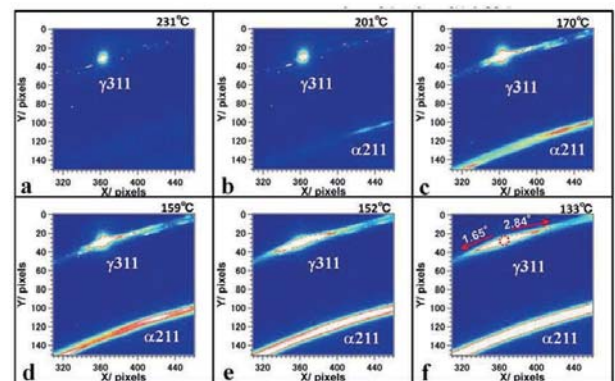


**Fig. 32** Change of diffraction pattern ( $\gamma 311$ ) in 14Cr-5Ni steel by the martensite transformation. [68]

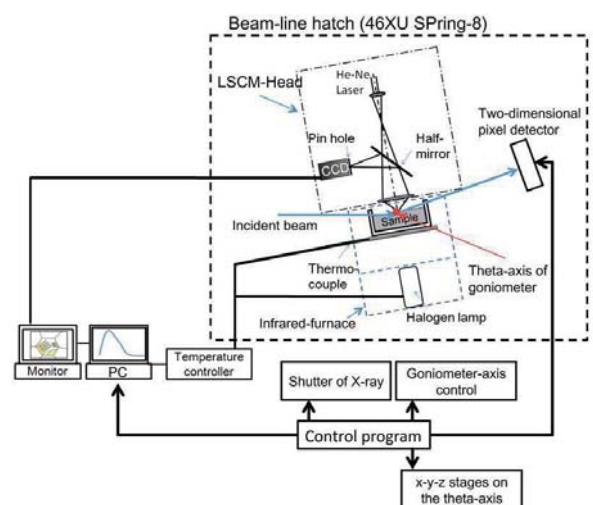


**Fig. 33** Hybrid in-situ observation system in real and reciprocal lattice space. [33]

beamline hatch. When the thermal cycles that simulate welding were programmed on the PC, the profiles were sent to the temperature controller, which reproduced the desired thermal cycles by switching the halogen lamp on and off, based on the measured temperature. Both the maximum heating and cooling rates of the system were 37 K s<sup>-1</sup>. The LSCM head enables in situ observations of microstructural changes at 30 frames/s at high temperatures. A charge coupled device camera was connected to the PC located outside the hatch, and the images were stored at a rate of 30 frames/s. The control program could trigger the temperature controller, the X-ray shutter, the x–y–z stages on h axis, goniometer axis control and the exposure of the pixel detector.

**Figure 34**[32] shows snapshots of the LSCM images for the LTT and MS specimens during the cooling cycle. In the case of the LTT, austenite was supercooled to 300 °C, as shown in Figure 34 LTT-(i). Further cooling caused a martensitic transformation, as shown in Fig. 34 LTT-(ii) and (iii). The image contrast of the precipitate was very clear because of the surface relief of the martensite. The yield stress increased linearly as the temperature decreased. Then the elastic strain balanced the transformation strain and it was effective in reducing the residual stress in the restricted weld. In the case of the MS, at 640 °C, a very weak contrast was observed on the grain boundary of the austenite and spread throughout the images at 550 °C, as shown in Figure 34 MS-(ii) and (iii). The nucleation site and the morphology of the precipitate were of the nature of a ferrite allotriomorph. The nucleation temperature should be higher than 640 °C because the magnification of LSCM images is 100. The image contrast of the ferrite allotriomorph was very weak because there was no relief on the surface of the specimen. The contrast in the LSCM image is affected by two factors: the formation of relief and a difference in reflectivity. In the case of relief formation, such as displacive transformation and thermal grooving at the grain boundary, the difference in the reflection direction of the laser light is responsible for the clear contrast in the LSCM image. On the other hand, in diffusional transformation, the contrast is very weak, as shown in Figure 34. This means that there is no surface relief, and the contrast is due to the differences of reflectivity between the ferrite and austenite. The light reflectivity is governed by the electrical conductivity. The difference of electrical conductivity between the ferrite and austenite should be small in the current chemical composition, and this difference causes a very weak contrast in the case of diffusional transformation. **Figure 35**[32] shows the d-spacing, time, temperature and intensity diagram (LTT-(a) and MS-(a)) during the phase transformations in the cooling cycle. The displayed reflection is that of austenite 1 1 1 and ferrite 1 1 0. The intensity was normalized. In the macro-view, the d-spacing of the austenite and ferrite decreased because of thermal shrinkage in the LTT and MS. When the phase transformation occurred, the intensity of the austenite decreased, as shown in Fig. 35. The marks (i), (ii) and

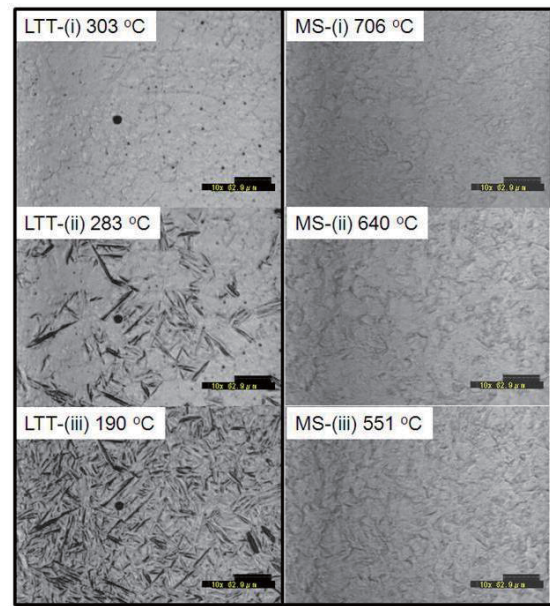


**Fig. 34** Microstructural changes for low-temperature-transformation material (LTT) and mild steel (MS). [32]

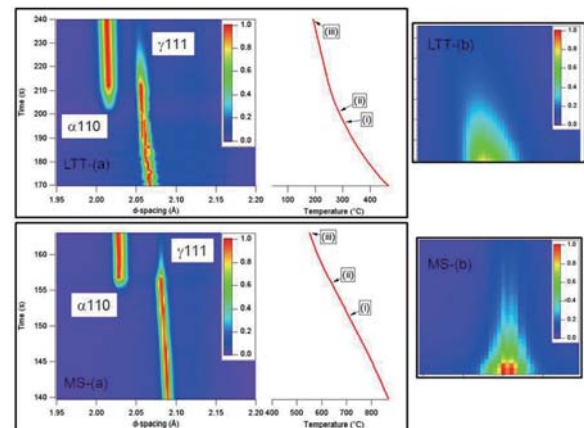


**Fig. 35** The d-spacing, time and temperature–intensity diagram during the cooling cycle in LTT (LTT-(a)) and MS (MS-(a)). [32]

(iii) in the temperature profile correspond to the number in Figure 34 for each steel sample. There was a discrepancy of approximately 20 °C between the surface temperature of the specimen and the thermocouple set behind the platinum plate stage. This discrepancy suggests that the LSCM images were compatible with the diffraction pattern. Hence, the developed system could follow the phase transformations in both real and reciprocal lattice space. Figure 35 LTT-(b) and MS-(b) show enlarged views of the austenite 1 1 1 diffraction peaks when the austenite decreased because of the phase transformations. The d-spacing continuously decreased along the trends in the macro-view in the LTT, whereas it increased against the trends in the MS. In order to analyze this phenomenon, a fit of Gaussian peaks [5] to the austenite reflection 1 1 1 was performed.

## 7. Summary

New techniques developed for direct observation of morphological evolution were introduced. They can be applied to the analysis of microstructural changes for improving control of weld properties. International cooperation in this field has just begun and first international workshop was held in 2010[70]. A second international workshop will be held at Osaka in 2012. Synchrotron based X-ray diffraction techniques combined with high-temperature laser scanning confocal microscopy; provide new and powerful tools for the study of phase transformations and microstructural evolution during welding. Continual improvements in synchrotron based methods can only increase the ability to monitor these transformations at higher spatial and temporal resolutions during welding. When combined with additional experiments and modelling, these techniques enable a deeper understanding of the kinetics of phase transformations.

## References

- [1] F. Matsuda, H. Nakagawa, J.-B. Lee, Quarterly Journal of The Japan Welding Society. 7 (1989) 229-234.
- [2] Y. Komizo, Welding Technology. 54 (2006) 55-59.
- [3] H. Chikama, H. Shibata, T. Emi, M. Suzuki, Materials Transactions Jim. 37 (1996) 620-626.
- [4] M. Reid, D. Phelan, R. Dippenaar, Isij International. 44 (2004) 565-572.
- [5] D. Phelan, M. Reid, R. Dippenaar, Computational Materials Science. 34 (2005) 282-289.
- [6] K. Nakama, Y. Haruna, J. Nakano, S. Sridhar, Isij International. 49 (2009) 355-364.
- [7] K. Yamamoto, H. Shibata, S. Mizoguchi, Isij International. 46 (2006) 82-88.
- [8] H. Mitsui, K. Oikawa, I. Ohnuma, R. Kainuma, K. Ishida, Isij International. 42 (2002) 1297-1302.
- [9] N. Yuki, H. Shibata, T. Emi, Isij International. 38 (1998) 317-323.
- [10] N. Kikuchi, S. Nabeshima, Y. Kishimoto, J. Nakano, S. Sridhar, Isij International. 48 (2008) 954-962.
- [11] H. Yin, T. Emi, H. Shibata, Acta Materialia. 47 (1999) 1523-1535.
- [12] F. Verhaeghe, J. Liu, M. Guo, S. Arnout, B. Blanpain, P. Wollants, Applied Physics Letters. 91 (2007) 124104 - 124104-03.
- [13] R. Trivedi, S.A. David, M.A. Eshelman, J.M. Vitek, S.S. Babu, T. Hong, T. DebRoy, Journal of Applied Physics. 93 (2003) 4885-4895.
- [14] H. Shibata, Y. Arai, M. Suzuki, T. Emi, Metallurgical and Materials Transactions B-Process Metallurgy and Materials Processing Science. 31 (2000) 981-991.
- [15] Y. Komizo, H. Terasaki, Science and Technology of Welding and Joining. 16 (2011) 56-60.
- [16] H. Terasaki, Y. Komizo, Science and Technology of Welding and Joining. 11 (2006) 561-566.
- [17] H. Terasaki, T. Yamada, Y.I. Komizo, Tetsu to Hagane-Journal of the Iron and Steel Institute of Japan. 93 (2007) 27-32.
- [18] Y. Komizo, Journal of the Japan Welding Society. 77 (2008) 26-31.
- [19] T. Yamada, H. Terasaki, Y. Komizo, Quarterly Journal of Japan Welding Society. 25 (2007) 416-420.
- [20] H. Terasaki, T. Yamada, Y. Komizo, Isij International. 48 (2008) 1752-1757.
- [21] D. Zhang, H. Terasaki, Y. Komizo, Journal of Alloys and Compounds. 484 (2009) 929-933.
- [22] T. Yamada, H. Terasaki, Y. Komizo, Science and Technology of Welding and Joining. 13 (2008) 118-125.
- [23] T. Yamada, H. Terasaki, Y. Komizo, ISIJ international. 49 (2009) 1059-1062.
- [24] S. Zhang, H. Terasaki, Y. Komizo, Tetsu to Hagane-Journal of the Iron and Steel Institute of Japan. 96 (2010) 64-69.
- [25] D. Zhang, H. Terasaki, Y. Komizo, Acta Materialia. 58 (2010) 1369-1378.
- [26] Y. Komizo, H. Terasaki, M. Yonemura, T. Osuki, Welding in the world-London-. 52 (2008) 56-63.
- [27] H. Terasaki, Y. Komizo, F. Nishino, M. Ikeda, Materials Science Forum, Trans Tech Publications Inc., 2008, pp. 21-24.
- [28] D. Zhang, H. Terasaki, Y. Komizo, Microscopy Research and Technique. 73 (2010) 67-70.
- [29] T. Yamada, H. Terasaki, Y. Komizo, Tetsu To Hagane-Journal of the Iron and Steel Institute of Japan. 96 (2010) 608-613.
- [30] Y. Komizo, H. Terasaki, Science and Technology of Welding and Joining. 16 (2011) 61-67.
- [31] S. Zhang, S. Morito, Y. Komizo, Tetsu To Hagane-Journal of the Iron and Steel Institute of Japan. 97 (2011) 399-405.
- [32] H. Terasaki, Y. Komizo, Scripta Materialia. 64 (2011) 29-32.
- [33] Y. Komizo, H. Terasaki, Science and Technology of Welding and Joining. 16 (2011) 79-86.
- [34] F. Banhart, In situ electron microscopy at high resolution, World Scientific Publishing Company, Singapore, 2008.
- [35] J. Basu, R. Divakar, J.P. Winterstein, N. Ravishankar, C.B. Carter, Microscopy and Microanalysis. 14 (2008) 246-247.
- [36] T. Imura, Microscopy Microanalysis Microstructures. 4 (1993) 101-110.
- [37] D.E. Newbury, D.B. Williams, Acta Materialia. 48 (2000) 323-346.
- [38] E.A. Torres, A.J. Ramirez, Science and Technology of Welding and Joining. 16 (2011) 68-78.
- [39] G. Shigesato, M. Sugiyama, Journal of Electron Microscopy. 51 (2002) 359-367.
- [40] J.W. Elmer, J. Wong, T. Ressler, Metallurgical and Materials Transactions a-Physical Metallurgy and Materials Science. 29 (1998) 2761-2773.
- [41] J.W. Elmer, J. Wong, T. Ressler, Metallurgical and Materials Transactions a-Physical Metallurgy and Materials Science. 32 (2001) 1175-1187.
- [42] J.W. Elmer, T.A. Palmer, J. Wong, Journal of Applied Physics. 93 (2003) 1941-1947.
- [43] J.W. Elmer, T.A. Palmer, Metallurgical and Materials Transactions a-Physical Metallurgy and Materials Science. 37A (2006) 2171-2182.
- [44] J.W. Elmer, T.A. Palmer, W. Zhang, B. Wood, T. DebRoy, Acta Materialia. 51 (2003) 3333-3349.
- [45] W. Zhang, J.W. Elmer, T. DebRoy, Science and Technology of Welding and Joining. 10 (2005) 574-582.
- [46] J.W. Elmer, J. Wong, T. Ressler, Scripta Materialia. 43 (2000) 751-757.
- [47] J.W. Elmer, T.A. Palmer, S.S. Babu, W. Zhang, T. DebRoy, Welding Journal. 83 (2004) 244S-253S.
- [48] J.W. Elmer, T.A. Palmer, S.S. Babu, W. Zhang, T. DebRoy, Journal of Applied Physics. 95 (2004) 8327-8339.
- [49] S.S. Babu, J.W. Elmer, J.M. Vitek, S.A. David, Acta Materialia. 50 (2002) 4763-4781.



## In-situ Observation Techniques of Solidification and Phase Transformation during Welding

- [50]T.A. Palmer, J.W. Elmer, S.S. Babu, Materials Science and Engineering a-Structural Materials Properties Microstructure and Processing. 374 (2004) 307-321.
- [51]J. Wong, T. Ressler, J.W. Elmer, Journal of Synchrotron Radiation. 10 (2003) 154-167.
- [52]J. Wong, M. Froba, J.W. Elmer, P.A. Waide, E.M. Larson, Journal of Materials Science. 32 (1997) 1493-1500.
- [53]Y. Komizo, T. Osuki, M. Yonemura, H. Terasaki, Transactions of JWRI. 33 (2004) 143-146.
- [54]T. Osuki, M. Yonemura, K. Ogawa, Y. Komizo, H. Terasaki, Science and Technology of Welding and Joining. 11 (2006) 33-42.
- [55]Y. Komizo, H. Terasaki, M. Yonemura, T. Osuki, Transactions of JWRI. 34 (2005) 51-55.
- [56]M. Yonemura, T. Osuki, H. Terasaki, Y. Komizo, M. Sato, A. Kitano, Materials Transactions. 47 (2006) 310-316.
- [57]H. Terasaki, Y. Komizo, M. Yonemura, T. Osuki, Metallurgical and Materials Transactions a-Physical Metallurgy and Materials Science. 37A (2006) 1261-1266.
- [58]Y. Komizo, H. Terasaki, M. Yonemura, T. Osuki, Quarterly Journal of The Japan Welding Society (2006) 57-64.
- [59]M. Yonemura, T. Osuki, H. Terasaki, Y. Komizo, M. Sato, H. Toyokawa, Materials Transactions. 47 (2006) 2292-2298.
- [60]Y. Komizo, H. Terasaki, Tetsu To Hagane-Journal of the Iron and Steel Institute of Japan. 94 (2008) 1-5.
- [61]T. Hashimoto, H. Terasaki, Y. Komizo, Science and Technology of Welding and Joining. 13 (2008) 409-414.
- [62]H. Terasaki, K. Yanagita, Y. Komizo, M. Sato, H. Toyokawa, Quarterly Journal of The Japan Welding Society. 27 (2009) 118s-121s.
- [63]C. Brönnimann, C. Bühler, E.F. Eikenberry, R. Horisberger, G. Hülsen, B. Schmitt, C. Schulze - Briesse, M. Suzuki, T. Tomizaki, H. Toyokawa, A. Wagner, Synchrotron Radiation News. 17 (2004) 23-30.
- [64]B. Schmitt, C. Bronnimann, E.F. Eikenberry, G. Hulsen, H. Toyokawa, R. Horisberger, F. Gozzo, B. Patterson, C. Schulze-Briesse, T. Tomizaki, Nuclear Instruments & Methods in Physics Research Section a-Accelerators Spectrometers Detectors and Associated Equipment. 518 (2004) 436-439.
- [65]B.E. Warren, X-ray diffraction, Courier Dover Publications, 1990.
- [66]S. Sasaki, KEK report. 90 (1990) 1-143.
- [67]W. Kurz, D.J. Fisher, Fundamentals of solidification, Trans Tech Publications, 1984.
- [68]S. Zhang, H. Terasaki, Y. Komizo, Tetsu To Hagane-Journal of the Iron and Steel Institute of Japan. 96 (2010) 691-697.
- [69]M. Yonemura, T. Osuki, H. Terasaki, Y. Komizo, M. Sato, H. Toyokawa, A. Nozaki, Journal of Applied Physics. 107 (2010) 013523-013523-6.
- [70]T. Kannengiesser, S.S. Babu, Y. Komizo, A.J.E. Ramirez, In-situ Studies with Photons, Neutrons and Electrons Scattering, Springer, 2010.